Errandonea, D.; Muñoz, A.; Rodríguez-Hernández, P.; Gomis, O.; Achary, SN.; Popescu, C.; Patwe, SJ.... (2016). High-pressure crystal structure, lattice vibrations, and band structure of BiSbO4. Inorganic Chemistry. 55(10):4958-4969. doi:10.1021/acs.inorgchem.6b00503.

High-pressure crystal structure, lattice vibrations, and band structure of $BiSbO_4$

Daniel Errandonea[†,], Alfonso Muñoz[‡], Placida Rodríguez-Hernández[‡], Oscar Gomis[§], S. Nagabhusan Achary[⊥], Catalin Popescu[∥], Sadeque J. Patwe[⊥], and Avesh K. Tyagi[⊥]*

[†]Departamento de Física Aplicada-ICMUV, Universidad de Valencia, MALTA Consolider Team, Edificio de Investigación, C. Dr. Moliner 50, 46100 Burjassot, Spain

[‡]Departamento de Física, MALTA Consolider Team and Instituto de Materiales y Nanotecnología, Universidad de La Laguna, 38206 La Laguna, Tenerife, Spain

[§]Centro de Tecnologías Físicas: Acústica, Materiales y Astrofísica, MALTA Consolider Team, Universitat Politècnica de València, Camí de Vera s/n, 46022 València, Spain

[⊥]Chemistry Division, Bhabha Atomic Research Centre, Mumbai 400 085, India

[∥]CELLS-ALBA Synchrotron Light Facility, Cerdanyola, 08290 Barcelona, Spain

ABSTRACT: The high-pressure crystal structure, lattice-vibrations, and electronic band structure of $BiSbO_4$ were studied by *ab initio* simulations. We also performed Raman spectroscopy, infrared spectroscopy, and diffuse-reflectance measurements, as well as synchrotron powder x-ray diffraction. High-pressure x-ray diffraction measurements show that the crystal structure of $BiSbO_4$ remains stable up to at least 70 GPa, unlike other known MTO_4-type ternary oxides. These experiments also give information on the pressure dependence of the unit-cell parameters. Calculations properly describe the crystal structure of $BiSbO_4$ and the changes induced by pressure on it. They also predict a possible high-pressure phase. A room-temperature pressure-volume equation of state is determined and the effect of pressure on the coordination polyhedron of Bi and Sb is discussed. Raman- and infrared-active phonons have been measured and calculated. In particular, calculations provide assignments for all the vibrational modes as well as their pressure dependence. In addition, the band structure and electronic density of states under pressure were also calculated. The calculations combined with the optical measurements allow us to conclude that $BiSbO_4$ is an indirect-gap semiconductor, with an electronic band gap of 2.9(1) eV. Finally, the isothermal compressibility tensor for $BiSbO_4$ is given at 1.8 GPa. The experimental (theoretical) data revealed that the direction of maximum compressibility is in the (0 1 0) plane at approximately 33º (38º) to the *c*-axis and 47º (42º) to the *a*-axis. The reliability of the reported results is supported by the consistency between experiments and calculations.

KEYWORDS: High pressure, Bismuth antimonate, XRD, Raman, FTIR, band gap, ab initio calculations.

1. Introduction

Recently there has been a large interest in the study of antimonate-based photocatalysts.[1] These compounds have been proposed for applications such a photocatalytic degradation of benzene and organic dyes.[2, 3] Among them $BiSbO_4$ is one of the most promising compounds.[4] The crystal structure of $BiSbO_4$ at ambient pressure has been accurately determined,[5] but only few of its Raman-active modes have been measured[6] and its infrared (IR)-active modes are not known yet. On the other hand, attempts have been made to determine the electronic band gap, but values ranging from 2.1 to 3.5 eV can be found in the literature.[1, 4, 7, 8]

During the last decade, intensive investigations have been carried out on the structural evolution of MTO_4-type ternary oxides under high-pressure (HP). They showed that compression is an efficient tool to improve the understanding of the main physical properties of vanadates,[9] phosphates,[10] chromates,[11] tungstates,[12] molydbates,[13] arsenates,[14] and many other MTO_4 compounds.[15] However, to the best our knowledge, an investigation of $BiSbO_4$ under pressure is still lacking in literature. On top of that, *ab initio* simulations have shown to be an accurate method to study the physical and chemical properties of compounds related to $BiSbO_4$.[16, 17] Usually these calculations provide an accurate description of such oxides as well as a better understanding of the experimental results and accurate predictions.

Based upon the facts described above we consider timely to perform and experimental and theoretical study of $BiSbO_4$ to deepen the knowledge on its properties and its behavior under compression. HP x-ray diffraction (XRD), Raman and infrared (IR) spectroscopy, and diffuse-reflectance experiments were carried out. The combination of calculations and experiments have allowed us to systematically study the structural, lattice-dynamics, and electronic properties of $BiSbO_4$, making a substantial progress in their understanding.

The paper is organized as follows: In the next section, we give a detailed description of the experimental techniques. The computational details are presented in Section 3. The results of experiments and calculations will be given in Section 4. Finally, the results of this work are summarized in Section 5.

2. Experimental methods

$BiSbO_4$ was prepared by solid state reaction of stoichiometric amounts of Bi_2O_3 and Sb_2O_3 in air. The reactants, Bi_2O_3 (Alfa Aesar, 99.99 %) and Sb_2O_3 (Alfa Aesar, 99 %) were heated at 600°C (6h) and 150 °C (2h) to remove any adsorbed moisture or volatile impurities. About 7g of homogenous mixture of Bi_2O_3 and Sb_2O_3 was pressed to a pellet of 1 inch diameter and 2mm thickness and heated at 600°C for 12 h and cooled slowly to room temperature (RT) at a rate of 1°C/min. The obtained product was re-homogenized and pressed again into pellets of about 10 mm diameter and 2 mm thickness and heated at 850°C for 24 h and cooled to RT at a rate of 1°C/min. All the heating procedures are carried out in air, where the Sb^{3+} is oxidized to Sb^{5+} by oxygen in air. The whitish product obtained after the final heat treatment was characterized and used for all the studies.

The composition of the synthesized material was determined by energy-dispersive x-ray spectroscopy carried out with a transmission electron microscope operated at 200 KeV. According with these measurements, in our sample, the content of Bi, Sb, and O atoms show no deviation from $BiSbO_4$ stoichiometry. Formation of single phase monoclinic $BiSbO_4$ (space group *I2/c*) was confirmed by powder XRD measurements. The XRD pattern at ambient conditions was recorded on a rotating anode based diffractometer using Cu K_α radiation. The

unit-cell parameters are in very good accordance with those determined by Enjalbert *et al.*[5] More details on the ambient-pressure structure will be given in the next section.

The Fourier-transform infrared (FTIR) absorption spectra of the sample were recorded from 400 to 4000 cm^{-1} on a JASCO Corp. FTIR spectrometer in transmission mode. Thin transparent pellets of a mixture of the sample and KBr were used for the FTIR studies. Raman spectra were collected in the backscattering geometry using a 488 nm Ar laser and a Jobin−Yvon spectrometer in combination with a thermoelectric-cooled multichannel CCD detector with spectral resolution below 2 cm^{-1}. A laser power of less than 10mW was used to avoid sample heating. Diffuse reflectance spectra were recorded by using an UV-VIS spectrometer (JASCO model V-530 spectrophotometer) using a finely powdered sample. From these measurements we determined the absorbance of $BiSbO_4$.

HP angle-dispersive powder XRD experiments were carried out using an Almax-Boehler diamond-anvil cell (DAC) with diamond culets of 280 μm. Before loading the DAC, the $BiSbO_4$ was ground in a mortar with a pestle to obtain a micrometer-sized powder. The pressure chamber was a 90 μm hole drilled on tungsten gasket pre-indented to 30 μm thickness. The studied sample was loaded in the pressure chamber together with a few micron-size ruby chips. The ruby fluorescence method[18] was used to determine pressure with an accuracy of 0.1 GPa. A 16:3:1 methanol-ethanol-H_2O mixture was used as pressure-transmitting medium.[19] Special care was taken during sample loading to occupy only a small fraction on the pressure chamber with the loaded sample to reduce the possibility of sample bridging between the diamond anvils.[20, 21] In situ HP XRD measurements at RT were carried out at the Materials Science and Powder Diffraction beamline (BL04-MSPD) of ALBA Synchrotron Light Source[22]. The incident monochromatic beam of wavelength 0.4246 Å was focused down to a 10 μm × 15 μm spot using

Kirkpatrick-Baez mirrors. A Rayonix CCD detector was used to collect XRD patterns. A clean-up pinhole was placed at 50 mm from the sample to reduce tails in the focused x-ray spot. A rocking (±3º) of the DAC was used at all pressures to obtain a homogeneous intensity distribution along Debye rings. The exposure time was 10 s for every acquisition. The two dimensional diffraction images collected were integrated with the FIT2D software.[23] Structural analyses were performed with PowderCell[24] and FullProf[25] software packages.

3. Overview of the calculations

Density-Functional Theory (DFT) total-energy calculations are a tested method that describes accurately the phase stability and the structural, dynamical, and electronic properties of semiconductors under pressure.[26] Ab initio total-energy simulations were performed to study $BiSbO_4$ under pressure and to determine its possible high pressure phase. The Vienna ab Initio Simulation package (VASP)[27] was employed to perform calculations within DFT[28] using the pseudopotential method. The full nodal character of the all-electron charge density in the core region was taken into account with the projector augmented wave scheme (PAW).[29] The electrons $5d^{10}$ $6s^2$ $6p^3$ of Bi were explicitly included in the calculations. Due to the O atoms, to achieve high precision results the set of plane waves was developed up to a large kinetic energy cutoff of 520 eV. The exchange-correlation energy was described in the generalized-gradient approximation (GGA) with the Perdew-Burke-Ernzenhof for solids (PBEsol) prescription.[30] Integrations within the Brillouin zone (BZ) were performed with dense grids of Monkhorst-Pack[31] k-special points appropriate to each structure. These ensure a convergence of 1 meV per formula unit for the total energy. For each considered structure and volume, the lattice parameters and atomic positions were fully optimized through the calculation of forces on the

atoms and the stress tensor. For the optimized structures the forces on the atoms were less than 0.004 eV/ Å and the deviation of the stress tensor components from the diagonal hydrostatic form lower than 0.1 GPa. The possible existence of phase transitions induced by pressure was considered in our calculations. The theoretical phase transitions and the transition pressures between the low and high pressure phases were determined by calculating the free energy of each phase as function of pressure.

Lattice dynamic calculations were carried out at the zone center (Γ) of the BZ with the direct force constant approach (or supercell method),[32] at several pressures. The construction of the dynamical matrix requires separate calculation of highly converged forces which arise due to fixed displacements of atoms from their equilibrium positions. The diagonalization of the dynamical matrix provides the frequency of the Raman and infrared modes. These calculations allow also identifying the symmetry and eigenvectors of the vibrational modes for the considered structure at the Γ point. The phonon density of states (DOS) was obtained with similar calculations using a (2 x 2 x 2) supercell. The knowledge of the PDOS allowed us to include temperature effects in the structural calculations. The quasi-harmonic approximation[33] was used to consider the zero point contribution and temperature effects on the phase transition at 300 K.

For completeness, electronic band structure calculations were carried out within the first BZ along the high-symmetry direction L-A-Γ-V-Z-M. Due to the heavy mass of Bi and Sb atoms the spin-orbit (SO) coupling is not negligible.[34] Therefore, calculations were made at selected pressures including the SO coupling. This extensively increases the computational time required for the simulation. However, only the results for the band-structure differs from the results obtained without considering the SO coupling. The effect of including the SO coupling in the calculation of phonon frequencies at Γ is negligible (small differences of 1-3 cm^{-1}).[35]

4. Results

a. Characterization at ambient conditions

The crystal structure of $BiSbO_4$ was accurately determined two decades ago by Enjalbert *et al.*[5] from single-crystal XRD measurements. The structure is shown in Figure 1. $BiSbO_4$ has a monoclinic structure and can be described in space group *I2/c*. It is formed by chains of SbO_6 octahedra, which share corners, forming a layer parallel to the (001) plane. The layers are held together by Bi atoms which are coordinated by eight O atoms, having the Bi coordination polyhedron four short and four long Bi-O bonds. We have confirmed the structure by Rietveld refinement using as starting parameters the reported structural parameters of Enjalbert *et al.*[5] The Rietveld refinement of the XRD pattern measured at ambient conditions is shown in Figure 2. The good matching of the observed and calculated intensities of XRD data, points toward a correct assignment of the crystal structure. The determined structural parameters are given in Tables 1 and 2. They agree within 0.2% with those reported in the literature.[5] The quality factors of the refinement are R_p = 2.76 %, R_{wp} = 3.51 %, R_F^2 = 5.78 %, and χ^2 = 1.07.

We will compare now our structural calculations with the experimental results. We have made *ab initio* total-energy calculations to determine the crystal structure of $BiSbO_4$. The calculated unit-cell parameters are given in Table 1. The agreement with the experimental data is excellent. In Table 2 we present the calculated atomic positions along with those obtained from the XRD study. The agreement between calculations and experimental results is again excellent. Both facts indicate that DFT calculations accurately describe the crystal structure of $BiSbO_4$ suggesting that DFT could be a powerful tool to calculate other physical properties.

We will discuss now the vibrational properties of $BiSbO_4$. From factor group analysis it can be established that the $BiSbO_4$-type structure presents 15 Raman-active phonons ($\Gamma = 8B_g +$

$7A_g$), 18 infrared (IR)-active phonons ($\Gamma = 9B_u + 9A_u$), and three acoustic phonons ($\Gamma = 2B_u + 1A_u$) at the zone center. Only four Raman-active modes have been earlier measured for $BiSbO_4$[6] and there is no report on IR-active modes in the literature. Here we report new Raman and IR experiments as well as lattice-dynamics calculations. Figure 3 shows the Raman spectrum of $BiSbO_4$ at ambient conditions. We have measured the expected fifteen modes. Their wave numbers are given in Table 3 and indicated by vertical ticks in Figure 3. Our wave numbers agree within experimental accuracy with those of the four modes that were previously measured.[6] In Figure 3 and Table 3, it can be seen that in the Raman spectrum there are four modes for wave numbers larger than 600 cm^{-1} and the rest of the modes are below 454 cm^{-1}. The Raman modes in the high-wavenumber region are weaker than the modes in the low-wavenumber region. For this reason, we magnified five times the Raman spectrum in the high-wavenumber region to facilitate the identification of the Raman modes on it. In the low-wavenumber region, there are two pairs of modes which partially overlap, making difficult their identification. We identify these modes with the help of calculations, which predict Raman modes very close in frequency near 135 cm^{-1} and 390 cm^{-1}. Taking this fact into account, we assumed that the asymmetric peaks found near these frequencies (which are the only two peaks that have a clear shoulder) correspond to a phonon doublet. We determined the frequency of each of the phonons of the doublet by making a Lorentzian multi-peak fitting analysis.[36] In order to illustrate this fact, we include in Figure 3 two insets (on the left-hand side) showing the asymmetric phonons and the two Lorentzian functions used to fit them.

In Table 3 we have also include the results of our calculations. There it can be seen that the agreement between measured (ω_{Exp}) and calculated (ω_{DFT}) Raman frequencies is quite good, much better than found in many related oxides.[37] This can be seen in Table 3 by looking to the

column that shows the relative difference between frequencies $R_\omega = (\omega_{Exp} - \omega_{DFT})/\omega_{Exp}$. The wavenumber of most modes agree within 5%. Only the A_g mode at 252 cm^{-1} and the B_g mode at 225 cm^{-1} show a slightly larger difference in wavenumber. The excellent agreement between experiments and calculations regarding Raman vibrations is illustrated in Figure 3, where in one inset we compare ω_{Exp} (empty symbols) and ω_{DFT} (solid symbols). Calculations have also allowed us to make a mode assignment, which is given in the Table 3. A_g and B_g modes have alternant frequencies. The Raman frequencies of niobates and tungstates related to $BiSbO_4$[38, 39] have been interpreted as internal modes associated to the NbO_6 (WO_6) octahedron, in which the center of mass does not move, and as external modes, in which the NbO_6 (WO_6) units move as rigid units. In general, the external modes occur at low wavenumbers. In addition, the internal stretching modes occur at the highest frequencies. A similar interpretation can be used for the Raman modes of $BiSbO_4$. According to our calculations, we tentatively assigned the four modes measured above 600 cm^{-1} to the internal modes of the SbO_6 octahedron. The pressure dependence of the Raman frequencies will be described in the next section; however, we would like to mention here that the internal modes of the SbO_6 octahedron have all similar and large pressure coefficients of the order of 4-5 cm^{-1}/GPa (see Table 3).

From our DFT calculations we have also determined the IR-active frequencies for $BiSbO_4$. To the best of our knowledge, there were no previous studies of IR modes for $BiSbO_4$. Table 4 shows the calculated wavenumber and assignment for the IR modes. Again, the modes can be divided in external and internal modes. The distribution of IR modes in frequency is qualitatively similar to the distribution of Raman modes. There are four modes at high frequency isolated from the rest of the modes. These modes are associated to internal vibrations of the SbO_6 octahedron. In addition to the calculations, we have carried out FTIR measurements in $BiSbO_4$.

The recorded transmittance spectrum is shown in Figure 4. The spectrum has two prominent absorption bands. One from 600 to 750 cm^{-1} which can be related to the four high-frequency modes and the corresponding calculated modes are located from 611 to 686 cm^{-1}. The second absorption band is from the cut-off of our FTIR setup, 400 cm^{-1}, to 525 cm^{-1}. This band can be associated to the cluster of four modes that our calculation predicts in between 370 and 502 cm^{-1}. Therefore, the calculated IR spectrum shows similitudes with the measured spectrum, although calculated frequencies are systematically slightly below the measured IR bands. However these differences are similar to those observed between experiments and calculations in other oxides.[17] The information obtained from our calculations is not only useful to interpret the present experiment, but also future experiments in which the frequency region would be extended below 400 cm^{-1}.

We will now discuss the results of the diffuse-reflectance experiments and the electronic structure calculations. Figure 5 shows the absorbance of the sample in the UV-VIS-NIR range. $BiSbO_4$ shows a steep absorption for energies higher than 2.9 eV. As we will comment below, $BiSbO_4$ is an indirect band-gap material. Assuming this hypothesis we determined the energy of the fundamental band gap (E_g) using a Tauc plot.[40, 41] In this plot $\sqrt{\alpha \cdot E}$ (where α is the absorbance) is expected to be proportional to the photon energy (E). This relation is fulfilled by the absorbance of $BiSbO_4$, as can be seen in the inset of Figure 5. The resulting plot has a distinct linear regime after the onset of absorption, which supports that $BiSbO_4$ is an indirect-band-gap semiconductor. Extrapolating the linear region to the abscissa in the Tauc plot yields the energy of the optical band gap of $BiSbO_4$. The value determined for the band-gap energy is E_g = 2.9(1) eV. This value is consistent with the experimental values reported by Lin *et al.* (E_g = 2.75 eV)[4] and by Li *et al.* (E_g = 2.96 eV),[8] confirming that $BiSbO_4$ is a wide-gap semiconductor. This

conclusion is also in agreement with *ab initio* calculations discussed latter. All these facts solve the controversies on the band gap of $BiSbO_4$ that exist in the literature and suggest that Muntean *et al.* have underestimated E_g (2.1 eV)[7] while You *et al.* has overestimated it (3.5 eV).[1]

The calculated band structure and electronic density of states (DOS) of $BiSbO_4$ at zero pressure are shown in Figures 6 and 7, respectively. According to our calculations, $BiSbO_4$ is an indirect band-gap material. The maximum of the valence band is at the Γ point of the Brillouin zone (BZ) and the minimum of the conduction band is at the Z point of the BZ. This fact is in agreement with the calculations reported by Lin *et al*.,[4] with the only difference that they place the maximum of the valence band in the middle of the Z-Γ line and not at Γ. On the other hand, those authors calculated a band gap of 3.5 eV[4] while we obtained a theoretical band gap of 2.62 eV, which is very close to the value determined from previous[4, 8] and present measurements (2.75 – 2.96 eV). It is well known that the calculated values of band gap are sensitive to exchange-correlation functionals. In the case of $BiSbO_4$, the excellent agreement between our calculations and experiments indicate that PBEsol gives an excellent performance for describing the electronic properties of $BiSbO_4$. In addition to the above described indirect band gap, from our calculations we determined that there are two direct band gaps very close in energy to the fundamental indirect band gap. The direct transitions are at the Z and Γ points of the BZ and the value of the direct band gaps are 2.69 and 2.90 eV, respectively. This agrees with the direct band gap reported by Li *et al.*[8]. However, these authors did not report any indirect band gap, which mislead their identification of $BiSbO_4$ as a direct gap material. One additional feature to remark of the band structure is that the dispersion of the valence bands is relatively small, with comparable dispersions along different directions. Regarding the composition of the bottom part of the conduction band and the top part of the valence band, in Figure 7 it can be seen that the

valence band in the range -4 to 0 eV is mainly composed of O 2p orbitals, however Bi 6s orbitals also contribute to the valence band in to some extent. On the other hand, the conduction band from 2.5 to 4.5 eV basically consists of O 2p, Sb 5s, and Bi 6p states.

b. High-pressure studies

Figure 8 shows selected XRD patterns measured in $BiSbO_4$ up to 70 GPa. We found that the patterns obtained from ambient pressure up to the highest pressure can be unequivocally assigned to the $BiSbO_4$-type structure. No new Bragg peaks indicative of a phase transition were observed in the XRD patterns up to 70 GPa. The quality of the XRD patterns allows the performance of Rietveld structural refinements[42] up to 17.8 GPa. Some examples of these refinements are shown in Figure 8. The R-factors of the refinement at 17.8 GPa are R_p = 3.12 % and R_{wp} = 5.97 %. Better refinements were obtained at lower pressures. From the refinements we have been able to determine not only the unit-cell parameters but also the free atomic positions. These allow us to evaluate how the interatomic distances are affected by pressure. Details of the procedure of the Rietveld refinement of the HP XRD patterns can be found elsewhere.[43] Beyond 17.8 GPa, due to a gradual peak broadening induced by the fact that the pressure medium is not quasi-hydrostatic anymore,[18, 44, 45] we assigned the XRD patterns to the $BiSbO_4$-type structure using the Le Bail method,[46] which allows us to extract information on how the unit-cell parameters evolve under compression.

The evolution of the unit-cell parameters and volume (see Figure 9) as a function of pressure obtained from experiments presents an excellent overall agreement with our *ab initio* calculations (see Figure 9). In particular, we found that up to 30 GPa the compression of $BiSbO_4$ is anisotropic, being the *c*-axis the most compressible axis. An explanation for this fact will be

provided while discussing the Bi-O and Sb-O bond compressibility. On the other hand, we also found that the β-angle considerably decreases up to nearly 30 GPa and then it becomes less affected by pressure. We have analyzed the pressure-volume (P-V) data obtained from the experiments using a third-order Birch-Murnaghan equation of state (EOS).[47] The fit was carried out using the EosFit7 software.[48] The obtained zero-pressure volume (V_0), bulk modulus (B_0), and its first-pressure derivative (B_0') are 310.3(6) Å^3, 149(6) GPa, and 3.5(2), respectively. The obtained value for the weighted $\chi 2$ in the EOS fit is 1.46. On the other hand, *ab initio* calculations give V_0 = 311.5(4) Å^3, B_0 = 109(2) GPa, $B_0' = 5.2(2)$. Apparently, calculations indicate that $BiSbO_4$ is more compressible than the experimental observations. This is also suggested in Figure 9 by the fact that the calculated volume crosses over the measured volume. The larger bulk modulus determined from the experiments could be related to the influence of non-hydrostaticity on the pressure dependence of unit-cell parameters[20], which could lead to EOS parameters which are not those ideally obtainable with a quasi-hydrostatic pressure media.

From the Rietveld refinements of the XRD patterns measured up to 17.8 GPa and from *ab initio* calculations we obtain very consistent information on bond distances and their pressure dependence. Since calculations also give this information up to 70 GPa, for the sake of briefness, we focused on the theoretical results for the further discussion. In Figure 1 we compare the $BiSbO_4$–type structure at 0 GPa with the same structure at 65 GPa. There it can be seen that the main change induced by pressure in the structure is the modification of the interlayer BiO_8 polyhedral units. In Table 5 we report the structural parameters of the calculated crystal structure at 73.3 GPa. By comparing it with Table 2, it can be seen that, with the exceptions of Sb atomic positions which are fixed by the symmetry of the structure, the atomic positions change when pressure is applied. In particular, the positions that change more are those of Bi and O_2. The

change of the atomic positions is related to the fact that BiO_8 polyhedral units are more compressible than SbO_6 octahedra. This fact can be easily understood by a quantitative comparison of the polyhedral compression. In Figure 10 we show the pressure dependence of the volume of the SbO_6 octahedron and BiO_8 polyhedron. These volumes and other parameters of the polyhedral units like the distortion index and effective coordination number (ECN) have been calculated using VESTA.[49] In the figure it can be seen that the relative change of the volume of the BiO_8 polyhedron is considerably larger than that of the SbO_6 octahedron. Indeed, using a 2nd order Birch-Murnaghan EOS a bulk modulus of 141(3) GPa is determined for BiO_8 while a bulk modulus of 304(5) GPa is determined for SbO_6. The later value is comparable with the bulk modulus of the stishovite phase of SiO_2,[50] one of the less compressible oxides that exists in nature. Therefore, the SbO_6 octahedral units can be considered as highly incompressible, and hence the larger BiO_8 units account for most of the volume reduction under compression. In particular, the relative change of the polyhedral volume of BiO_8 is comparable with the relative change of the unit-cell volume of $BiSbO_4$. We would like to recall here that the Raman modes associated to internal vibrations of the SbO_6 octahedron tend to have large pressure coefficients. This observation is fully consistent with the fact that the SbO_6 octahedron is highly incompressible.

The different polyhedral compressibility is also the cause of the anisotropic compression of $BiSbO_4$. By looking at the crystal structure in Figure 1, it can be followed that in order to compress the *a*- and *b*-axis it is necessary to compress the layers of SbO_6 octahedra. However, the *c*-axis can be easily reduced by compressing the BiO_8 polyhedra, which is the reason for this axis to be the most compressible one. In Figure 10, it can be also seen that beyond 30 GPa, the compressibility of BiO_8 is reduced and becomes similar to that of SbO_6 (their P-V curves

become nearly parallel). This is due to the fact that the bond distance of the "soft" Bi-O bonds at low pressure is easily reduced. However, as pressure increase and the Bi-O distances decrease, the strength of the bonds increases, due to electrostatic repulsions, making the Bi-O bonds as "hard" as the Sb-O bonds. This is a typical phenomenon of layered materials[51] that combine "soft" and "hard" bonds. It qualitatively explains the observed reduction in the compressibility of the *c*-axis beyond 30 GPa.

From Figure 10 we can also get information on how the different polyhedral units are modified by pressure. In the case of SbO_6, the distortion index (defined in Ref. 49) remains smaller than 0.012 in the whole pressure range covered by the studies. In addition, the ECN of this polyhedron stays always very close to 6. From this it can be concluded that the SbO_6 remains nearly regular up to 70 GPa, and the effect of pressure on it is a gradual and small reduction of its volume. The small volume reduction can be illustrated by the fact that the average Sb-O bond length is reduced from 1.962Å at ambient pressure to 1.892Å at 70 GPa. In the case of BiO_8 the situation is quite different. The polyhedron becomes considerably more regular and the ECN increases from 4 at ambient pressure to 6 at 70 GPa. This is basically because the four long Bi-O bonds [2.830 Å (x2) and 3.032(9) Å (x2)] of the BiO_8 polyhedron are more compressible than the four short Bi-O bonds [2.232 Å(x2) and 2.238 Å (x2)]. This is a consequence of the important change of the atomic coordinates of O_2 that we discussed above. In particular, due to the large compressibilities of the Bi-O bonds, it is possible to consider that at 70 GPa Bi is 6 + 4 coordinated in contrast to ambient pressure where Bi is 4 + 4 coordinated. At 70 GPa the Bi-O bond distances are: 2.125 Å (x2), 2.154 Å (x2), 2.317Å (x2), 2.741 Å (x2), and 2.862 Å (x2). In particular, most of the compression of the Bi-O bonds takes place up to 30 GPa. As can be seen in Figure 10, at this pressure the ECN reaches already a value close to 5.5. The "easy"

compression of the Bi-O up to 30 GPa is related to the change of compressibility of the *c*-axis observed at 30 GPa as we described above.

From our results it can be concluded the $BiSbO_4$ is probably one of the MTO_4 compounds with a larger pressure range of stability. Phase transitions in phosphates are induced by pressure between 20 and 40 GPa,[10] in tungstates and molybdates below 25 GPa,[12, 13, 15] in silicates near 20 GPa,[52] in vanadates below 10 GPa,[9] and in chromates even at lower pressures.[11] We think the large pressure stability of $BiSbO_4$ is caused by its layered structure, which thanks to the large compressibility of Bi-O bonds can accommodate the increasing repulsive and stearic stresses induced by pressure by deforming the irregular BiO_8 polyhedra, thereby avoiding the transformation to a high-pressure phase.

Let us comment now on the effect of pressure on theoretical Raman and IR phonons. It can be seen in Tables 3 and 4 that according with the calculations, the highest frequency modes are systematically more sensitive to compression. As we commented above, this is consistent with the low compressibility of the SbO_6 octahedron. On the other hand, we found that all Raman modes harden under compression, which is typical for oxides. On the contrary, there are two IR modes which have negative pressure coefficients. In spite of this fact, these two modes (one A_u mode and one B_u mode) cannot be considered as classical soft-modes, because if results are extrapolated, pressure has to go beyond 450 GPa to make at least the wavenumber one of the two modes to reach zero.[53] The results given in Tables 3 and 4 can be useful for comparison with future HP Raman and/or IR experiments. The Grüneisen parameters ($\gamma = \frac{B_0}{\omega_0}\frac{\partial \omega}{\partial P}$) of the different modes are given for completeness. They were calculated assuming B_0 = 109 GPa.

Before concluding the discussion of the effects of pressure in the physical properties of $BiSbO_4$, we will comment on the evolution of the band gap energy (E_g) with pressure, which is

shown in Figure 11. As already commented, $BiSbO_4$ has an indirect Γ-Z band gap. This band gap grows almost linearly with a pressure coefficient at zero pressure of $\frac{\partial E_g}{\partial P} = 0.082$ eV/P. The direct Γ–Γ band gap follows as similar pressure dependence. However, as compression increases, the top of the valence band moves faster toward higher energies at the Z point than at the Γ point. As a consequence of it, at 11GPa an indirect-to-direct band-gap crossover takes place and $BiSbO_4$ becomes a direct band gap semiconductor. The direct gap at Z-Z evolves in a quadratic form with a pressure coefficient at zero pressure of $\frac{\partial E_g}{\partial P} = 0.068$ eV/P.

To conclude this section we would like to comment that we have theoretically searched the existence of possible HP phases in $BiSbO_4$. It is know that the structurally related fergusonite-type $NdTaO_4$ can be transformed into a $LaTaO_4$-type structure (space group $P2_1/c$) by the combined application of pressure (8 GPa) and temperature (1500 ºC).[54] In order to determine if a similar phase transition can take place in $BiSbO_4$ we have calculated at 300 K the free energy of the candidate HP structure and compared it with the free energy of the initial $BiSbO_4$-type phase. The postulated HP structure is shown in Figure 1. The results of the free-energy calculations are shown in Figure 12. On it, the free-energy difference between both phases is plotted (taking $BiSbO_4$ as a reference). There it can be seen that beyond 52 GPa the $LaTaO_4$-type phase is predicted to become thermodynamically more stable than the $BiSbO_4$–type phase; hence a phase transition is likely to take place. This conclusion is in apparent contradiction with the fact that experiments found the $BiSbO_4$–type structure to remain stable at least up to 70 GPa. The fact that the XRD pattern measured at 70 GPa cannot be assigned to the proposed HP as shown in Figure 8, where the position of the calculated Bragg peaks of the HP phase are at very different positions that the Bragg peaks of the $BiSbO_4$ structure. One possible reason for this is apparent discrepancy is the presence of large kinetic barriers which hinder the occurrence of the phase

transition. This is quite common in phase transitions induced by pressure that involve a large atomic rearrangement and a large volume collapse. This is the case of the transition predicted here. The transition involves a 10 % volume collapse and an increase of the coordination number of both the Bi and Sb atoms. The hindering of the theoretically proposed phase transition due to a high kinetic barrier is also consistent with the fact that the proposed transition needs a major reconstruction of the crystal structure and puckering of octahedral layers (compare both structures a 65 GPa in Figure 1). In order to check the kinetic barrier hypothesis, the combined application of pressure and temperature will be needed, as observed in $NaTaO_4$[54] and $BiPO_4$[55]. In both compounds heating beyond 1500 K was needed to trigger HP phase transitions. We hope our theoretical predictions will stimulate such studies in the near future. To facilitate comparison with our theoretically predicted HP structure, its structural details are given in Table 5.

c. Isothermal compressibility tensor

The isothermal compressibility tensor, β_{ij}, is a symmetric second rank tensor which relates the state of strain of a crystal to the change in pressure that induced it.[56] The tensor coefficients for a monoclinic crystal with ***b*** as the unique crystallographic axis are:

$$\beta_{ij} = \begin{pmatrix} \beta_{11} & 0 & \beta_{13} \\ 0 & \beta_{22} & 0 \\ \beta_{13} & 0 & \beta_{33} \end{pmatrix}$$

We have obtained the isothermal compressibility tensor coefficients for $BiSbO_4$ at 1.8 GPa using the IRE (Institute of Radio Engineers) convention for the orthonormal basis for the tensor: $e_3 \| c$, $e_2 \| b^*$, $e_1 \| e_2 \times e_3$. The tensor has been obtained with the linear Lagrangian approximation by means of the equations given in Ref. 57 and with the infinitesimal Lagrangian approximation as implemented in the WinStrain package.[58] In the linear Lagrangian approximation a linear fit of the unit-cell parameters was carried out in the pressure range 0 - 3.6 GPa where the variation of

the unit-cell parameters with pressure was found to be linear. Table 6 includes the values of the lattice parameters at zero pressure and their pressure derivatives from the linear fits, which are used in the linear Lagrangian approximation, for the case of our experimental and *ab initio* calculated data. Table 6 also reports the β_{ij} coefficients of the isothermal compressibility tensor with the two approximations used. The β_{ij} coefficients obtained with the linear Lagrangian approximation agree, within the experimental uncertainties, with those obtained with the infinitesimal Lagrangian approximation as expected according to our small-strains assumption. On the other hand, it can be observed that there is a qualitative agreement between the experimental and calculated β_{ij} coefficients because $\beta_{33} > \beta_{11} > \beta_{22}$ in both cases. The fact that β_{33} is the larger coefficient is a consequence of the large compressibility of *c*-axis. However, when comparing theory with experiments, the theoretical β_{ij} coefficients are greater than the experimental counterparts. This result indicates that at low pressure (1.8 GPa) the theoretically calculated unit-cell is more compressible than the unit-cell experimentally determined. These differences are consistent with the differences observed between experiments and calculation described and discussed in the previous section.

The eigenvalues (λ_i, i =1-3) and eigenvectors (ev_i, i = 1-3) for the isothermal compressibility tensor are reported in Table 6. Taking into account the eigenvalues, it is found that for our experiments with the linear Lagrangian approximation, the maximum, intermediate and minimum compressibilities are 4.97(17) $\times$ 10^{-3}, 1.32(12) $\times$ 10^{-3}, and 0.20(9) $\times$ 10^{-3} GPa^{-1}, respectively; whereas for the case of our calculations the obtained values for the compressibilities are 7.03 $\times$ 10^{-3}, 1.84 $\times$ 10^{-3} and 1.10 $\times$ 10^{-3} GPa^{-1}. These experimental (theoretical) results indicate that around 77% (71%) of the total compression over the pressure range 0 - 3.6 GPa, is being accommodated along the direction of maximum compressibility.

Taking into account the eigenvector ev_1, the major compression direction occurs in the (0 1 0) plane at the given angle Ψ (see Table 6) to the *c*-axis (from *c* to *a*). Note that the direction of maximum compressibility, considering the value of β, is at approximately 33º (38º) to the *c* axis and 47º (42º) to the *a*-axis for the case of our experimental (theoretical) study. The direction of intermediate compressibility given by eigenvector ev_2 is along the *b*-axis, and the direction of minimum compressibility given by eigenvector ev_3 is in the (0 1 0) plane perpendicular to the direction of maximum compressibility. To conclude, we highlight that there is a reasonably good agreement between the directions of maximum, intermediate, and minimum compressibility given by our experimental and theoretical compressibility tensors.

5. Concluding remarks

In this work we reported an experimental and theoretical study of the physical properties of $BiSbO_4$ at ambient pressure and under compression. Our studies have allowed us to analyze the structural, vibrational, and electronic properties of this compound. We found that calculations accurately reproduce the crystal structure of $BiSbO_4$. They also were useful to deepen the understanding of the electronic and vibrational properties. In particular, calculations have helped us for the assignment of phonon modes and allowed us to predict where future experiments may find the IR-active modes. The pressure dependences of the different Raman and IR modes are also reported. On top of that, the study of the electronic structure has demonstrated that $BiSbO_4$ is an indirect band-gap material, with a band gap in the visible of 2.9(1) eV. Information on the band structure and its pressure dependence is also reported. Regarding high pressure studies, x-ray diffraction experiments together with calculations have allowed us to determine that the initial phase remains stable up to very high pressure. The room-temperature equation of state of

this phase is also reported together with the pressure dependence of the unit-cell parameters. From experiments [calculations] we determined V_0 = 310.3(6) Å^3, B_0 = 149(6) GPa, and B_0' = 3.5(2) [V_0 = 311.5(4) Å^3, B_0 = 109(2) GPa, B_0' = 5.2(2)]. The fact that experiments leads to a smaller compressibility could be related to the influence of non-hydrostaticity in the experiments. The pressure dependence of the unit-cell volume is discussed on the light of the effect of pressure on BiO_8 and SbO_6 polyhedra. Additionally, calculations predict a phase transition beyond 52 GPa, which is not observed in the experiments. A possible cause for this is the presence of a kinetic barrier which might have hindered the finding of the transition as observed previously in related oxides. Finally, the isothermal compressibility tensor is given for the low-pressure phase at 1.8 GPa and its eigenvalues and eigenvectors are obtained providing information about the directions of maximum, intermediate and minimum compressibilities. We feel the results here reported will stimulate additional high-pressure studies in $BiSbO_4$ and related oxides.

AUTHOR INFORMATION

Corresponding Author

*E-mail: daniel.errandonea@uv.es

Author Contributions

The manuscript was written through contributions of all authors. All authors have given approval to the final version of the manuscript.

Notes

The authors declare no competing financial interests.

ACKNOWLEDGMENT

Research supported by the Spanish government MINECO under Grants No: MAT2013-46649-C4-1/2/3-P and MAT2015-71070-REDC. We also acknowledge the computer time provide by MALTA cluster and the Red Española de Supercomputación. Experiments were performed at MSPD beamline at ALBA Synchrotron Light Facility with the collaboration of ALBA staff.

Table Captions

Table 1: Calculated (DFT) and measured (Exp) unit-cell parameters and volume for $BiSbO_4$. Experimental parameters from the literature[5] are also included for comparison.

Table 2: Calculated (DFT) and experimental (Exp) atomic positions for $BiSbO_4$. Wyckoff positions of different atoms are indicated in the left column. The experimental positions reported in the literature (Ref. 5) are also included for comparison.

Table 3: Experimental (ω_{Exp}) and calculated (ω_{DFT}) Raman modes of $BiSbO_4$ (in cm^{-1}) including mode assignment. The relative difference between measured and calculated frequencies is also given (R_ω) as well as the calculated pressure coefficients, $d\omega_{DFT}/dP$ (in cm^{-1}/GPa), and the Grüneisen parameter (γ). Phonon frequencies from Ref. 6 are included for comparison.

Table 4: Calculated frequencies (ω) of the IR modes (in cm^{-1}) including mode assignment. The pressure coefficients ($d\omega/dP$) are also given (in cm^{-1}/GPa) as well as the Grüneisen parameter (γ).

Table 5: Structural parameters of the low-pressure crystal structure calculated at 73.3 GPa.

Table 6: Structural details of the theoretically predicted HP phase at 70 GPa.

Table 7: Lattice parameters at zero pressure, their pressure derivatives, the isothermal compressibility tensor coefficients, β_{ij}, and their eigenvalues, λ_i, and eigenvectors, ev_i, for $BiSbO_4$ at 1.8 GPa. The results are given using the linear Lagrangian and the infinitesimal Lagrangian methods with data from our experiments and our theoretical calculations.

Figure Captions

Figure 1: Crystal structure of $BiSbO_4$ at ambient pressure and 65 GPa, and of $LaTaO_4$-type $BiSbO_4$ at 65 GPa.

Figure 2: Powder XRD pattern of $BiSbO_4$ at ambient conditions (λ = 1.5417 Å). Experiment: dots. Rietveld refinement: solid line. Vertical ticks indicate the position of Bragg reflections. The residual of the refinement is also shown.

Figure 3: Raman spectra of $BiSbO_4$ at ambient conditions. The high-frequency region is magnified (x5) to better show the modes of this region. Ticks show the identified Raman modes. In the figure, there are two insets (on the left-hand side) to show that two peaks consist of a doublet of modes. The black lines show the region of interest of the measured Raman spectrum and the color lines are the two phonons assigned (the ticks indicate their wavenumbers). A third inset (on the right-hand side of the figure) compares calculated (solid symbols) and measured (empty symbols) frequencies. In this inset, for the horizontal axis the experimental wavenumbers are used.

Figure 4: FTIR spectrum of $BiSbO_4$ at ambient conditions. Vertical ticks indicate the calculated frequencies.

Figure 5: Absorption spectrum of $BiSbO_4$. The inset shows the Tauc plot used to determine E_g. The red line shows the extrapolation of the linear region to the abscissa.

Figure 6: Calculated band structure of $BiSbO_4$ at 0 GPa.

Figure 7: Total and partial electronic density of states of $BiSbO_4$ at 0 GPa. The black line corresponds to the total DOS.

Figure 8: Selection of XRD patterns measured at different pressures. The dots are the experimental results and the solid lines the refinements (Rietveld for the three lowest pressures and Le Bail for the three highest pressures). The residuals of the refinements are also shown. The vertical ticks indicate the positions of the Bragg peaks. At 70 GPa the ticks show the calculated Bragg peaks for the low-pressure (LP) and postulated high-pressure (HP) phases to illustrate that the XRD pattern can be assigned to the LP phase but not to the predicted HP phase.

Figure 9: (Top) Pressure dependence of the unit-cell parameters. The inset shows the results obtained for the β angle. (Bottom) Pressure dependence of the unit-cell volume. Symbols: experiments. Solid lines: calculations. The dashed line in the bottom plot represents the 3rd order EOS fitted to the experimental results.

Figure 10: (Top) Relative variation of the unit-cell and polyhedral volumes with pressure. (Center) Distortion index of the SbO_6 octahedron and BiO_8 polyhedron as a function of pressure. (Bottom) Effective coordination number of Bi and Sb versus pressure.

Figure 11: Evolution of direct Γ-Γ, Z-Z, and indirect Z-Γ band-gap energy with pressure.

Figure 12: Free energy difference between the $BiSbO_4$-type and $LaTaO_4$-type structure as a function of pressure. The free energy of the $BiSbO_4$-type structure is taken as a reference.

REFERENCES

(1) You, Q.; Fu, Y.; Ding, Z.; Wu, L.; Wang, X.; Li, Z. *Dalton. Trans.* **2011**, *40*, 5774 – 5780.

(2) Xu, Y.J.; Zhuang, Y.B.; Fu, X.Z. *J. Phys. Chem. C* **2010**, *114*, 2669 – 2676.

(3) Zeng, J; Liu, S.L.; Cai, J.; Zhang, N.L. *J. Phys. Chem. C* **2010**, *114*, 7806 - 7811.

(4) Lin, X.P.; Huang, F.Q.; Wang, W.D.; Zhang, K.L. *Appl. Catal. A* **2006**, *307*, 257 - 262.

(5) Enjalbert, R.; Sorokina, S.; Castro, A.; Galy, J. *Acta Chem. Scand.* **1995**, *49*, 813 - 819.

(6) Wang, S.F.; Hsu, H.F.; Wang, Y.R.; Huang, Y.H. *J. Eur. Ceram. Soc.* **2011**, *31*, 2975 – 2980.

(7) Muntean, S.; Zhitar, V.; Volodina, G.; Pavlenko, V.; Shemyakova, T. *Moldavian Journal of Physical Sciences* **2009**, *8*, 283 – 286.

(8) Li, H.L.; Wang, X.J.; Yuan, J.L.; Zhao, J.T.; Yang, X.X.; Zhang, Z.J.; Chen, H.K.; Zhang, G.B.; Shi, C.S. *Chin. Phys. Lett.* **2008**, *25*, 3790 – 3793.

(9) Garg, A.B.; Errandonea, D.; Rodríguez-Hernández, P.; López-Moreno, S.; Muñoz, A.; Popescu, C. *J. Phys.: Condens. Matter* **2014**, *26*, 265402.

(10) Lacomba-Perales, R.; Errandonea, D.; Meng, Y.; Bettinelli, M. *Phys. Rev. B* **2010**, *81*, 064113.

(11) Bandiello, E.; Errandonea, D.; Martinez-Garcia, D.; Santamaria-Perez, D.; Manjon, F.J. *Phys. Rev. B* **2012**, *85*, 024108.

(12) Gomis, O.; Sans, J.A.; Lacomba-Perales, R.; Errandonea, D.; Meng, Y.; Chervin, J.C.; Polian, A. *Phy. Rev. B* **2012**, *86*, 054121.

(13) Errandonea, D.; Gracia, L.; Lacomba-Perales, R.; Polian, A.; Chervin, J.C. *J. Appl. Phys.* **2013**, *113*, 123510.

(14) Errandonea, D.; Kumar, R. S.; Lopez-Solano, J.; Rodrıguez-Hernandez, P.; Muñoz, A.; Rabie, M. G.; Saez Puche, R. *Phys. Rev. B* **2011**, *83*, 134109.

(15) Errandonea, D.; Manjon, F.J. *Prog. Mat. Sci.* **2008**, *53*, 711 – 773.

(16) Lopez-Moreno, S.; Errandonea, D.; Rodriguez-Hernandez, P.; Muñoz, A. *Inorg. Chem.* **2015**, *54*, 1765−1777.

(17) Errandonea, D.; Muñoz, A.; Rodríguez-Hernández, P.; Proctor, J.E.; Sapiña, F.; Bettinelli, M. *Chem. Inorg.Chem.* **2015**, *54*, 7524 – 7535.

(18) Mao, H.K.; Xu, J.; Bell, P.M. *J. Geophys. Res.* **1986**, 91, 4673 - 4676.

(19) Klotz, S.; Chervin, J.C.; Munsch, P.; Marchand, G.L. *J. Phys. D: Appl.* **2009**, *42*, 075413.

(20) Errandonea, D.; Muñoz, A.; Gonzalez-Platas, J. *J. Appl. Phys.* **2014**, *115*, 216101.

(21) Errandonea, D. *Crystal Research and Technology* **2015**, *50*, 729 – 736.

(22) Fauth, F.; Peral, I.; Popescu, C.; Knapp, M. *Powder Diffr.* **2013**, *28*, S360 – S370.

(23) Hammersley, A.P.; Svensson, S.O.; Hanfland, M.; Fitch, A.N.; Häusermann, D.; *High Pressure Res.* **1996**, *14*, 235 - 248.

(24) Kraus W.; Nolze, G. *J. Appl. Crystallogr.* **1996**, *29*, 301 - 303.

(25) Rodrıguez-Carvajal, J. *Physica B* **1993**, *192*, 55 - 69.

(26) Mujica, A.; Rubio, A.; Muñoz, A.; Needs, R.J. *Rev. Mod. Phys.* **2003**, *79*, 863 - 912.

(27) Kresse, G.; Hafner, J. *Phys. Rev. B* **1993**, *47*, 558 - 561.

(28) Hohenberg, P.; Kohn, W. *Phys. Rev.* **1964**, *136*, B864 – B871.

(29) Kresse, G.; Joubert, D. *Phys. Rev. B* **1999**, *59*, 1758 - 1775.

(30) Perdew, J.P.; Ruzsinszky, A.; Csonka, G.I.; Vydrow, O.A.; Scuseria, G.E.; Constantin, L.A.; Zhou, X.; Burke, K. *Phys. Rev. Lett.* **2008**, *100*, 136406.

(31) Monkhorst, H.J. Pack, J.D. *Phys. Rev. B* **1976**, *13*, 5188 - 5192.

(32) Parlinski, K. Computer Code PHONON. See: http://wolf.ifj.edu.pl/phonon.

(33) Baroni, S.; de Gironcoli, S.; Dal Corso, A.; Giannozzi, P. *Rev. Mod. Phys.* **2001**, *73*, 515 - 562.

(34)Yu, P.; Cardona, M. Fundamentals of Semiconductors, 2nd edition; Springer-Verlag: Berlin, 2003.

(35) O. Gomis, R. Vilaplana, F.J. Manjón, P. Rodríguez-Hernández, E. Pérez-González, A. Muñoz, V. Kucek, and C. Drassar, *Phys. Rev. B* **2011**, *84*,174305.

(36) Errandonea, D.; Gracia, L.; Lacomba-Perales, R.; Polian, A.; Chervin, J.C. *J. Appl. Phys.* **2013**, *113*, 123510.

(37) Ruiz-Fuertes, J.; Lopez-Moreno, S.; Lopez-Solano, J.; Errandonea, D.; Segura, A.; Lacomba-Perales, R.; Muñoz, A.; Radescu, S.; Rodrıguez-Hernandez, P.; Gospodinov, M.; Nagornaya, L.L.; Tu, C.Y. *Phys. Rev. B* **2012**, *86*, 125202.

(38) Jehng. J. M.; Wachs, I. E. *Chem. Mater.* **1991**, *3*, 100 - 107.

(39) Manjón, F.J.; López-Solano, J.; Ray, S.; Gomis, O.; Santamaría-Pérez, D.; Mollar, M.; Panchal, V.; Errandonea, D.; Rodríguez-Hernández, P.; Muñoz, A. *Phys. Rev. B* **2010**, *82*, 035212.

(40) Tauc, J. *Mater. Res. Bull.* **1968**, *3*, 37 - 46.

(41) Errandonea, D.;Popescu, C.; Garg, A.B.; Botella, P.; Martinez-Garcıa, D.; Pellicer-Porres, D.; Rodrıguez-Hernandez, P.; Muñoz, A.;Cuenca-Gotor, V.; Sans, J. A. *Phys. Rev. B* **2016**, *93*, 035204.

(42) Rietveld, H. M. *Journal of Applied Crystallography* **1969**, *2*, 65 – 71.

(43) Errandonea, D.; Santamaria-Perez, D.; Grover, V.; Achary, S.N.; Tyagi, A.K. *J. Appl. Phys.* **2010**, *108*, 073518.

(44) Errandonea, D.; Ferrer-Roca, C.; Martınez-Garcia, D.; Segura, A.; Gomis, O.; Muñoz, A.; Rodrıguez-Hernandez, P.; Lopez-Solano, J.; Alconchel, S.; Sapiña, F. *Phys. Rev. B* **2010**, *82*, 174105.

(45) Errandonea, D.; Meng, Y.; Somayazulu, M.; Häusermann, D. *Physica B* **2005**, *355*, 116 − 125.

(46) LeBail, A. *Powder Diffraction* **2005**, *20*, 316 - 326.

(47) Birch, F. *Phys. Rev.* **1947**, *71*, 809.

(48) Angel, R. J.; Alvaro, M.; Gonzalez-Platas, J. *Z. Kristallog.* **2014**, *229*, 405 - 419.

(49) Momma, K.; Izumi, F. *J. Appl. Crystallogr.* **2011**, 44, 1272 - 1276.

(50) Panero, W.R.; Benedetti, L.R.; Jeanloz, R. *J. Geophys. Res.* **2003**, *108*, 2015 – 2022.

(51) Schwarz, U.; Goñi, A. R.; Syassen, K.; Cantarero, A.; Chevy, A. *High Pressure Research*, **1992**, *8*, 396 – 398.

(52) Knittle, E.; Williams, Q. *American Mineralogist* **1993**, *78*, 245 - 252.

(53) Errandonea, D.; Pellicer-Porres, J.; Pujol, M.C.; Carvajal, J.J.; Aguiló, M. *J. Alloys Compd.* **2015**, 638, 14 – 20.

(54) Titov, Y. A.; Sych, A. M.; Sokolov, A. N.; Kapshuk, A. A.; Markiv, V. Y., Belyavina, N. M. *J. Alloys Compd.* **2000**, *311*, 252 – 255.

(55) Errandonea, D.; Gomis, O.; Santamaría-Perez, D.; García-Domene, B.; Muñoz, A.; Rodríguez-Hernández, P.; Achary, S. N.; Tyagi, A. K.;Popescu, C. *J. Applied Phys.* **2015**, *117*, 105902.

(56) Haussühl, S. *Physical Properties of Crystals. An Introduction*; Wiley-VCH, Weinheim, 2007.

(57) Knight, K. S.; *Phys. Chem. Minerals* **2010**, *37*, 529 - 533.

(58) Angel,R. J. http://www.rossangel.com/text_strain.htm

Table1

	DFT	Exp.	Exp.[5]
a (Å)	5.49537	5.4689(1)	5.4518(8)
b (Å)	4.93617	4.8889(1)	4.8784(4)
c (Å)	11.77221	11.8224(2)	11.825(1)
β (º)	100.9686	101.05(2)	101.11(1)
V (Å^3)	313.500	310.23(2)	308.6(1)

Table 2

Atom		x	y	z
Bi (4e)	DFT	0	0.50549	0.25
	Exp.	0	0.51100(25)	0.25
	Exp.[5]	0	0.5125	0.25
Sb (4a)	DFT	0	0	0
	Exp.	0	0	0
	Exp.[5]	0	0	0
O_1 (8f)	DFT	0.11797	0.84194	0.15441
	Exp.	0.1293(18)	0.8531(18)	0.1511(8)
	Exp.[5]	0.121(3)	0.841(3)	0.155(2)
O_2 (8f)	DFT	0.24044	0.29542	0.06555
	Exp.	0.2499(19)	0.2970(19)	0.0599(8)
	Exp.[5]	0.240(3)	0.292(3)	0.062(2)

Table 3

Mode	ω_{Exp}	ω_{Exp}[6]	ω_{DFT}	R_ω	$d\omega_{DFT}/dP$	γ
B_g	783	788	746.4	0.0467	3.92	0.57
A_g	730		751.7	-0.0297	4.18	0.61
B_g	636		602.5	0.0528	4.02	0.73
A_g	603		569.4	0.0557	4.95	0.95
B_g	452	454	457.9	-0.0131	2.99	0.71
A_g	420		437.6	-0.0419	2.77	0.69
B_g	394	397	399.9	-0.0150	4.51	1.23
A_g	387		386.9	0.0003	4.12	1.16
B_g	319		305.5	0.0423	0.66	0.24
A_g	252	256	235.6	0.0651	3.58	1.66
B_g	225		208.8	0.0720	0.71	0.37
A_g	158		152.2	0.0367	2.84	2.03
B_g	137		136.0	0.0073	1.07	0.86
A_g	133		134.8	-0.0135	1.29	1.04
B_g	56		56.0	0	1.13	2.20

Table 4

Mode	ω	dω/dP	γ
A_u	686.27	4.31	0.68
B_u	653.95	4.36	0.73
A_u	626.20	4.78	0.83
B_u	611.42	4.47	0.80
A_u	501.68	2.91	0.63
B_u	416.92	3.71	0.97
A_u	391.47	5.15	1.43
B_u	370.39	2.76	0.81
A_u	312.25	1.36	0.47
B_u	272.05	0.70	0.28
A_u	262.05	1.13	0.47
B_u	245.60	1.30	0.58
A_u	240.23	-0.25	-0.11
A_u	200.21	0.47	0.26
B_u	185.86	-0.44	-0.26
B_u	151.20	0.80	0.58
A_u	117.31	0.90	0.84
B_u	72.85	0.99	1.48

Table 5

a = 4.93294 Å, b = 4.35412 Å, c = 10.79405 Å, β = 97.2255º			
Atom	x	y	z
Bi (4e)	0	0.54684	0.25
Sb (4a)	0	0	0
O_1 (8f)	0.12221	0.85622	0.16076
O_2 (8f)	0.18229	0.35214	0.06580

Table 6

a = 7.05898 Å , b = 5.04331 Å, c = 7.27652 Å, and β = 121.0207º			
Atom	x	y	z
Bi (4e)	0.16640	0.25000	0.08322
Sb (4e)	0.33235	0.76801	0.41617
O_1(4e)	0.19898	0.75004	0.09949
O_2(4e)	0.05802	0.9905	0.27903
O_3(4e)	0.50001	0	0.33126
O_4(4e)	0.34341	0.38625	0.42171

Table 7

Method	Linear Lagrangian		Infinitesimal Lagrangian	
	Experiment	Theory	Experiment	Theory
a_0 (Å), da/dP (Å·GPa^{-1})	5.469(3), -0.0133(20)	5.4954, -0.0245(15)		
b_0 (Å), db/dP (Å·GPa^{-1})	4.889(2), -0.0064(4)	4.9352, -0.0091(3)		
c_0 (Å), dc/dP (Å·GPa^{-1})	11.822(2), -0.0427(14)	11.7722, -0.056(4)		
β_0 (°), dβ/dP (°·GPa^{-1})	101.05(9), -0.276(13)	100.969, -0.37(3)		
β_{11} (10^{-3} GPa^{-1})	1.56(19)	3.34	1.6(3)	3.35
β_{22} (10^{-3} GPa^{-1})	1.32(8)	1.84	1.34(17)	1.83
β_{33} (10^{-3} GPa^{-1})	3.61(12)	4.79	3.65(16)	4.82
β_{13} (10^{-3} GPa^{-1})	-2.15(20)	-2.87	-2.3(3)	-3.15
λ_1 (10^{-3} GPa^{-1})	4.97(17)	7.03	5.2(3)	7.32
ev_1 (λ_1)	(0.53, 0, -0.85)	(0.61, 0, -0.79)	(0.55, 0, -0.84)	(0.62, 0, -0.78)
λ_2 (10^{-3} GPa^{-1})	1.32(12)	1.84	1.34(17)	1.83
ev_2 (λ_2)	(0, 1, 0)	(0, 1, 0)	(0, 1, 0)	(0, 1, 0)
λ_3 (10^{-3} GPa^{-1})	0.20(9)	1.10	0.10(8)	0.85
ev_3 (λ_3)	(0.85, 0, 0.53)	(0.79, 0, 0.61)	(0.84, 0, 0.55)	(0.78, 0, 0.62)
Ψ (°)[a]	147.7(1.3)	142.1	146.9(1.6)	141.6

[a] The major compression direction occurs in the (0 1 0) plane at the given angle Ψ to the c axis (from c to a).

Figure 1

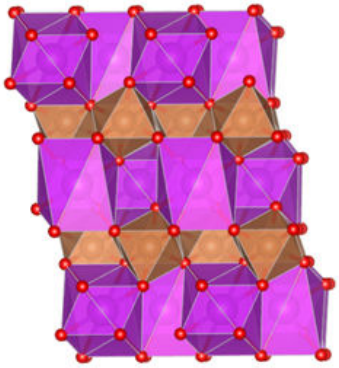

$BiSbO_4$-type ambient pressure

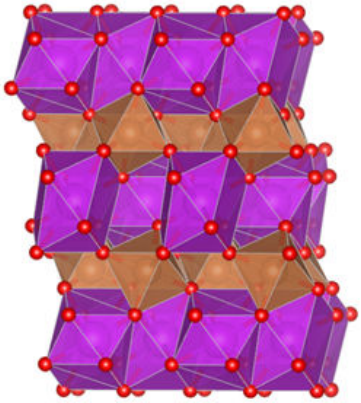

$BiSbO_4$-type 65 GPa

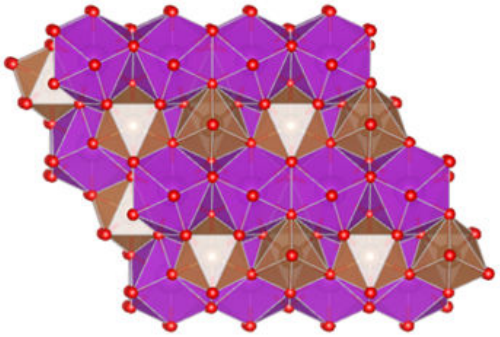

$LaTaO_4$–type 65 GPa

Figure 2

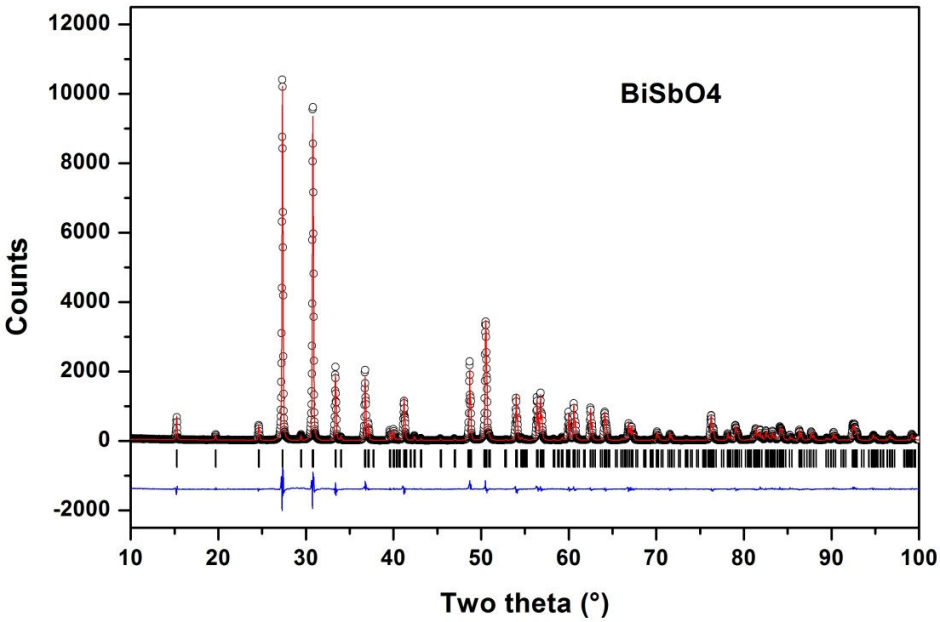
BiSbO4
Counts
Two theta (°)
12000
10000
8000
6000
4000
2000
0
-2000
10
20
30
40
50
60
70
80
90
100

Figure 3

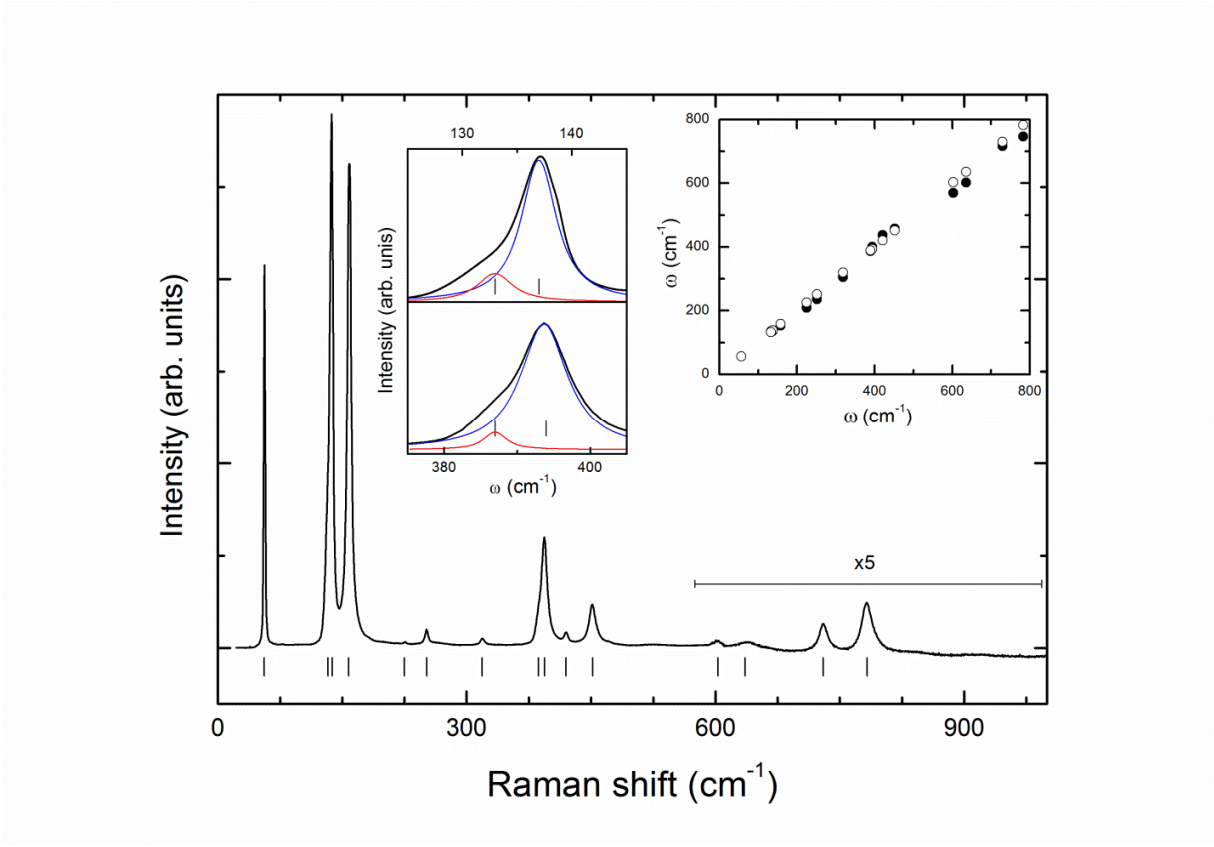
Intensity (arb. units)
Raman shift (cm-1)
0
300
600
900
x5
130
140
Intensity (arb. unis)
380
400
ω (cm-1)
800
600
400
200
0
ω (cm-1)
0
200
400
600
800
ω (cm-1)

Figure 4

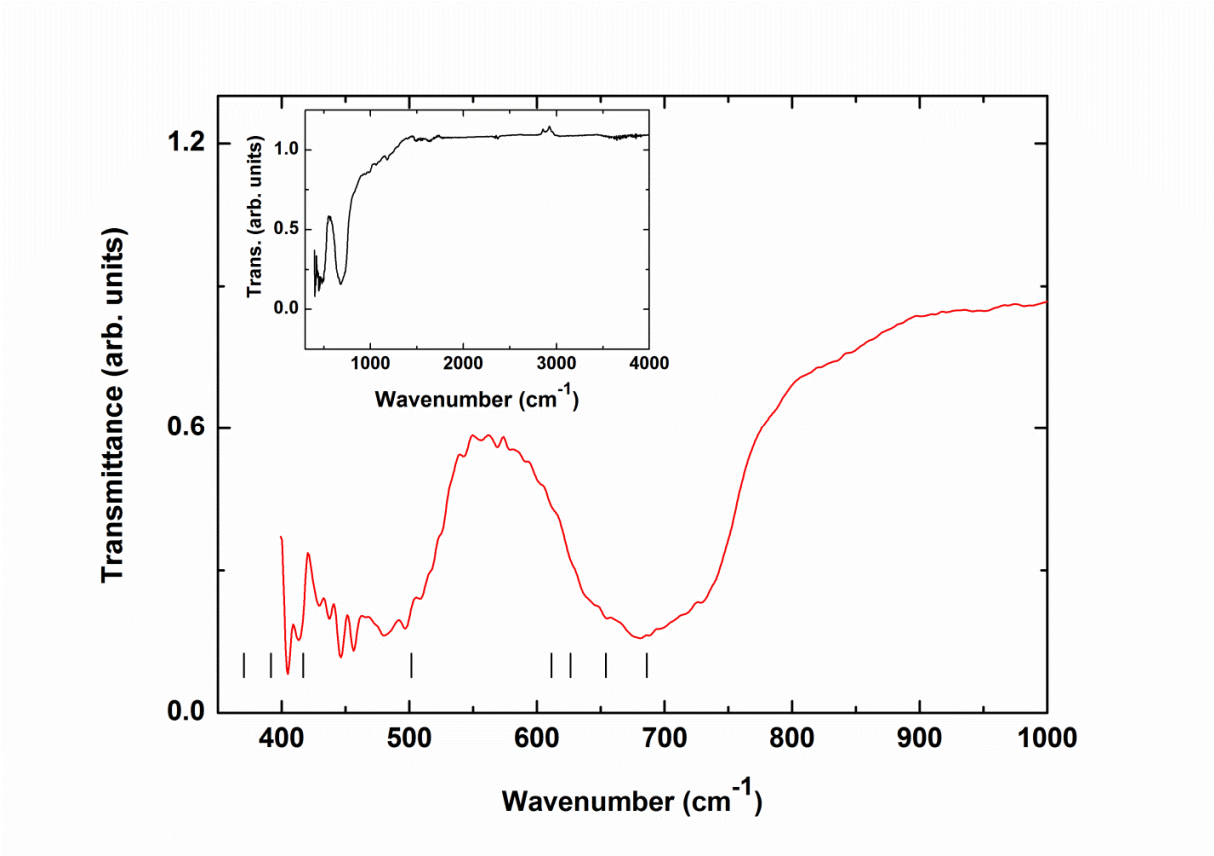
Transmittance (arb. units)
1.2
0.6
0.0
400
500
600
700
800
900
1000
Wavenumber (cm-1)
Trans. (arb. units)
1.0
0.5
0.0
1000
2000
3000
4000
Wavenumber (cm-1)

Figure 5

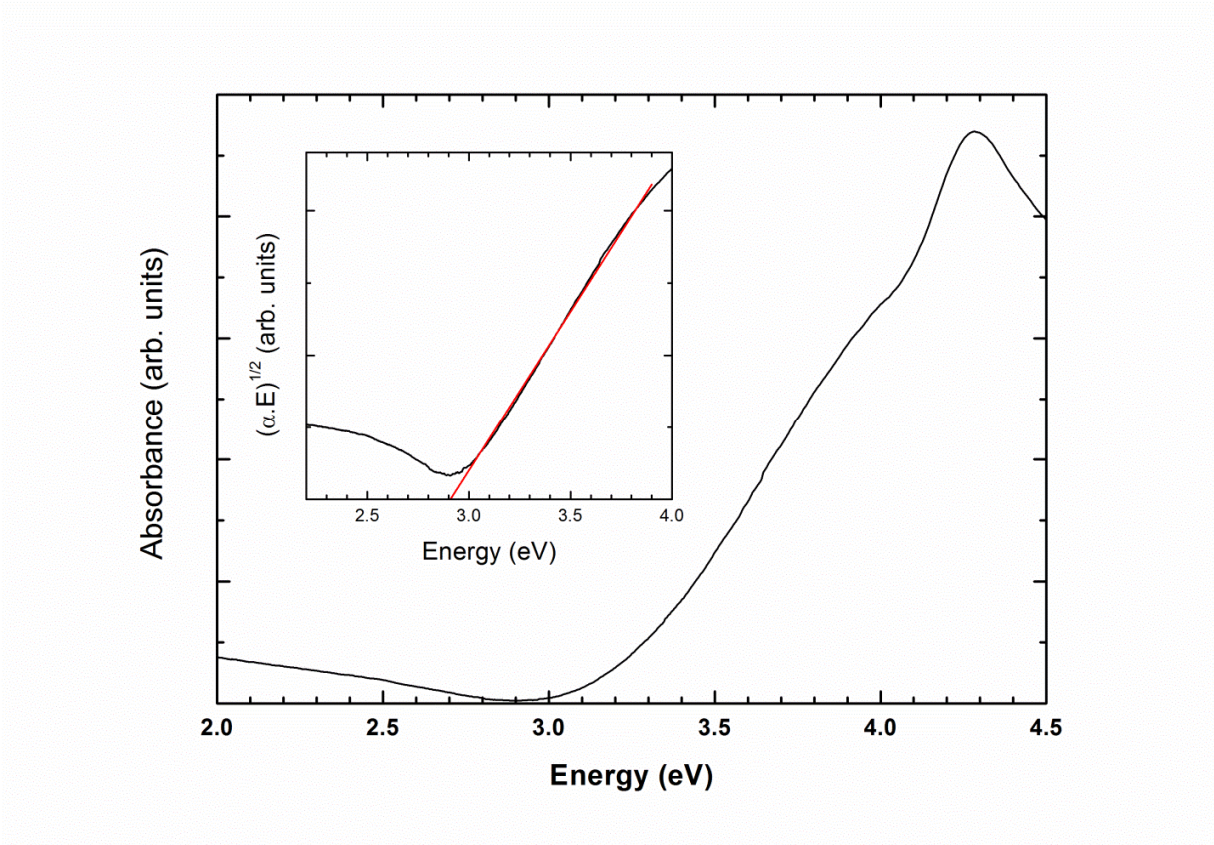
Absorbance (arb. units)
2.0
2.5
3.0
3.5
4.0
4.5
Energy (eV)
(α.E)^1/2 (arb. units)
2.5
3.0
3.5
4.0
Energy (eV)

Figure 6

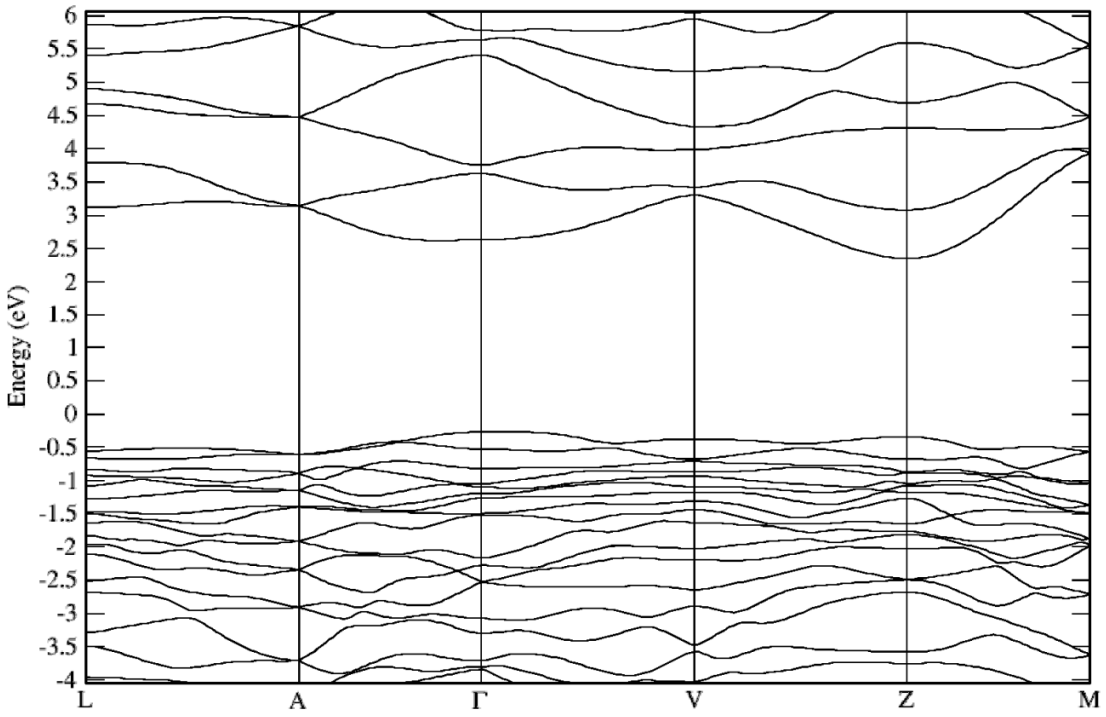

Figure 7

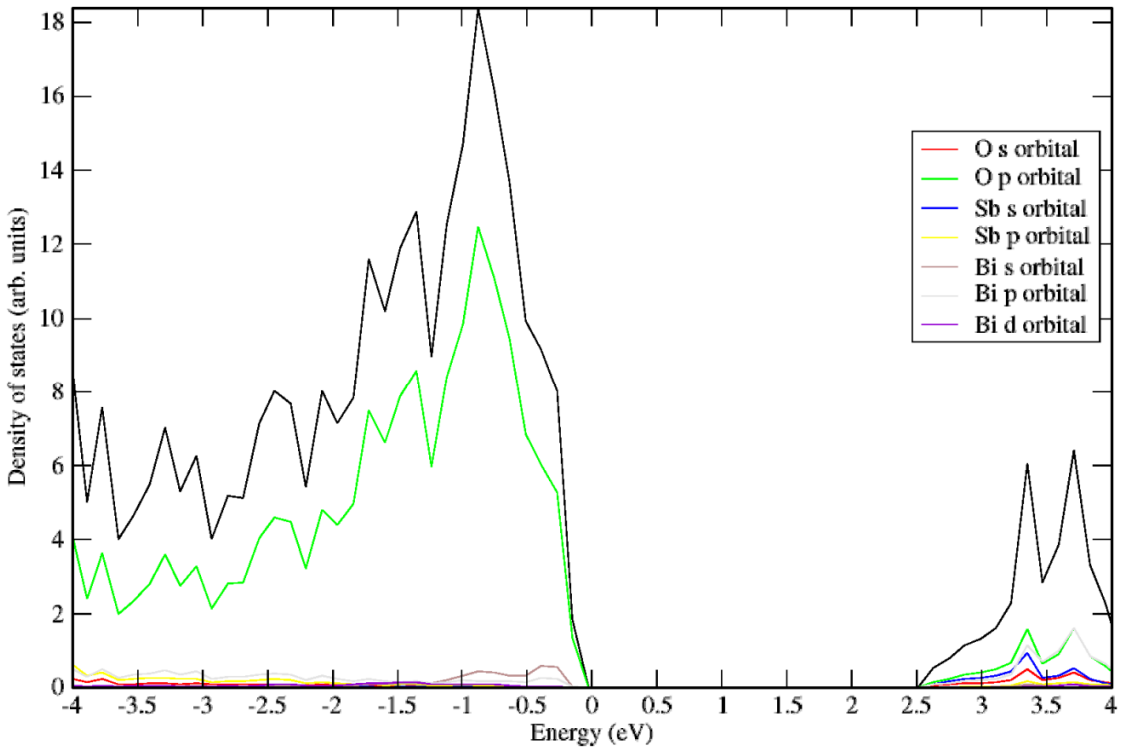
Density of states (arb. units)
Energy (eV)
O s orbital
O p orbital
Sb s orbital
Sb p orbital
Bi s orbital
Bi p orbital
Bi d orbital

Figure 8

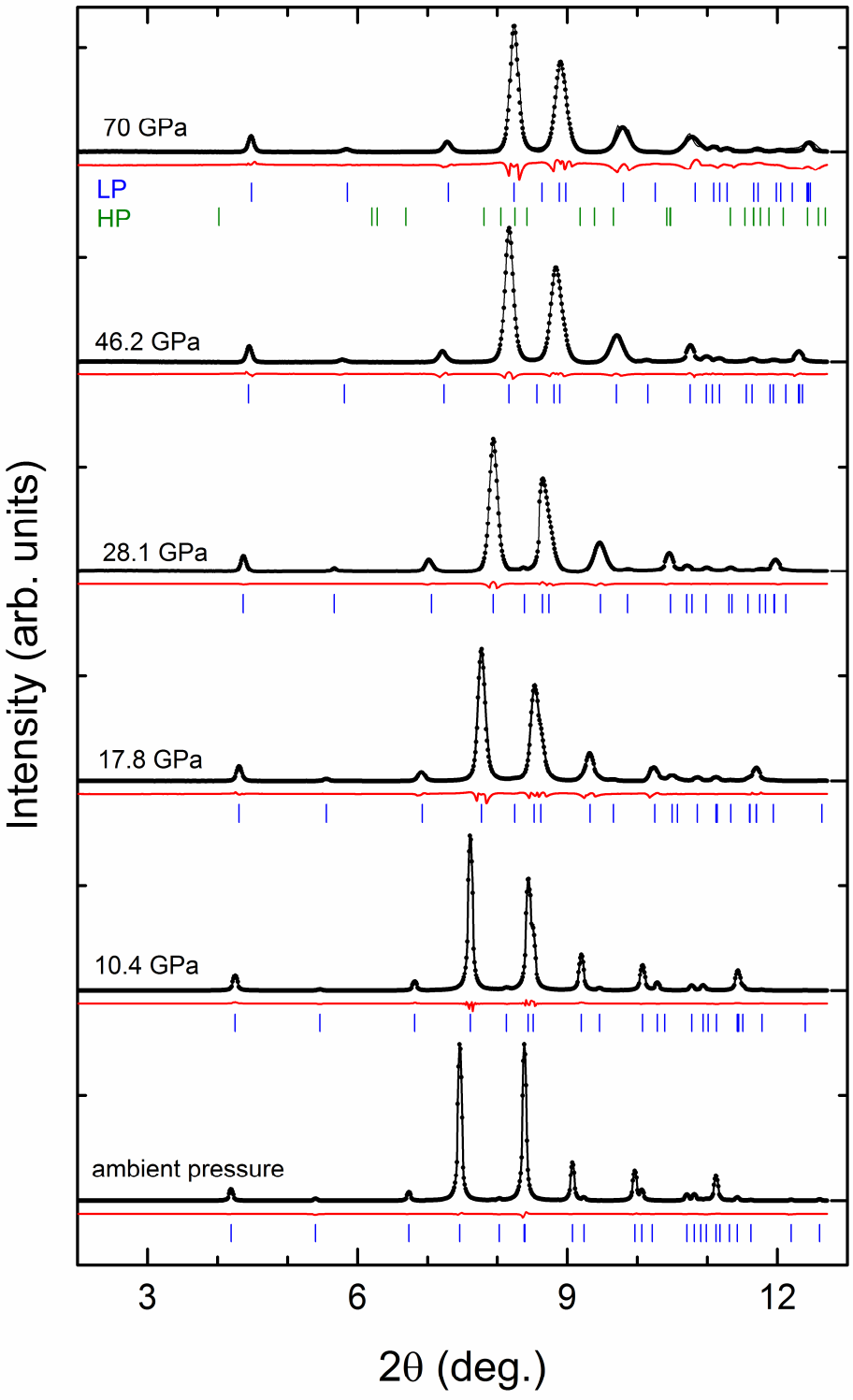
70 GPa
LP
HP
46.2 GPa
28.1 GPa
17.8 GPa
10.4 GPa
ambient pressure
Intensity (arb. units)
3
6
9
12
2θ (deg.)

Figure 9

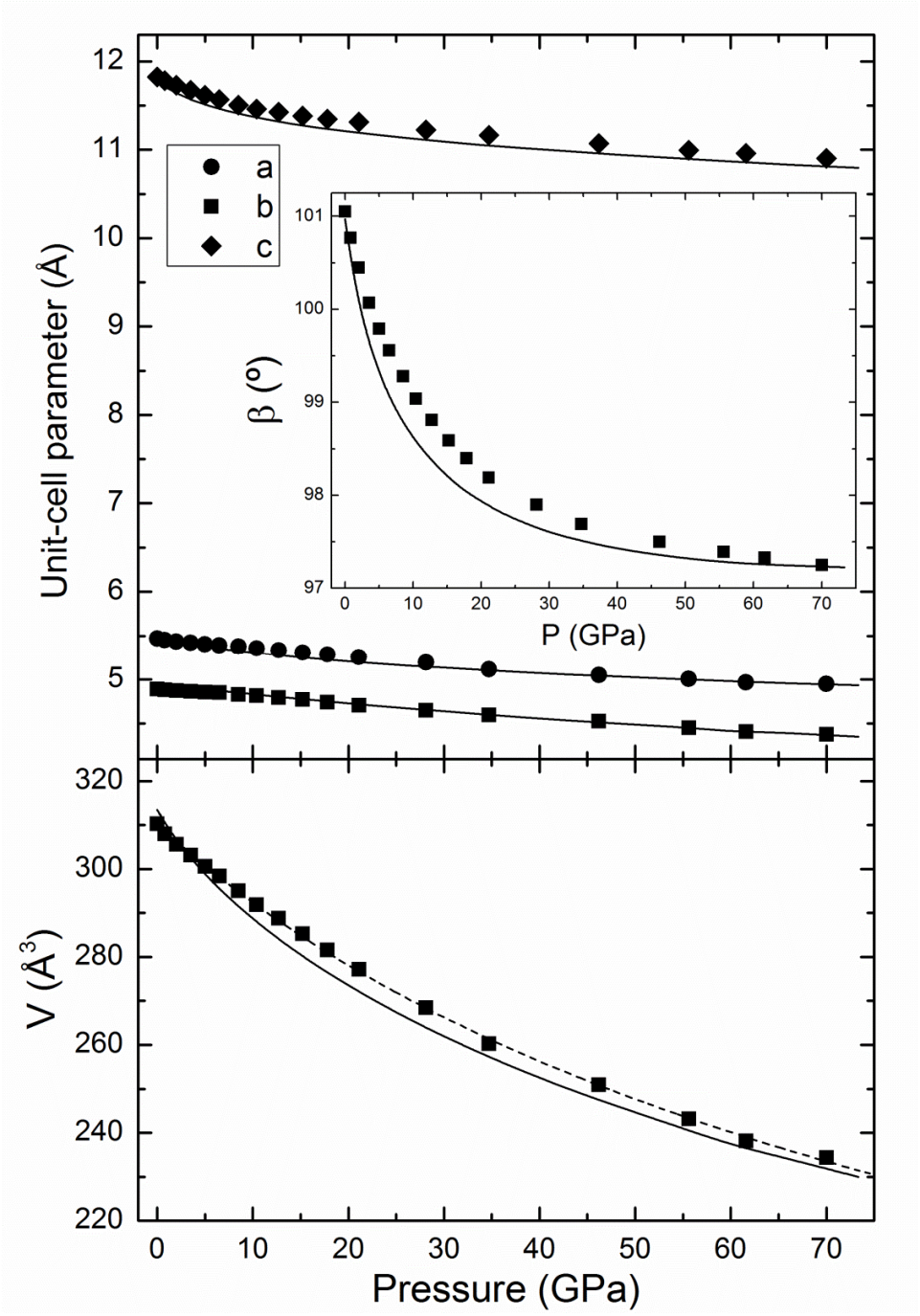

Figure 10

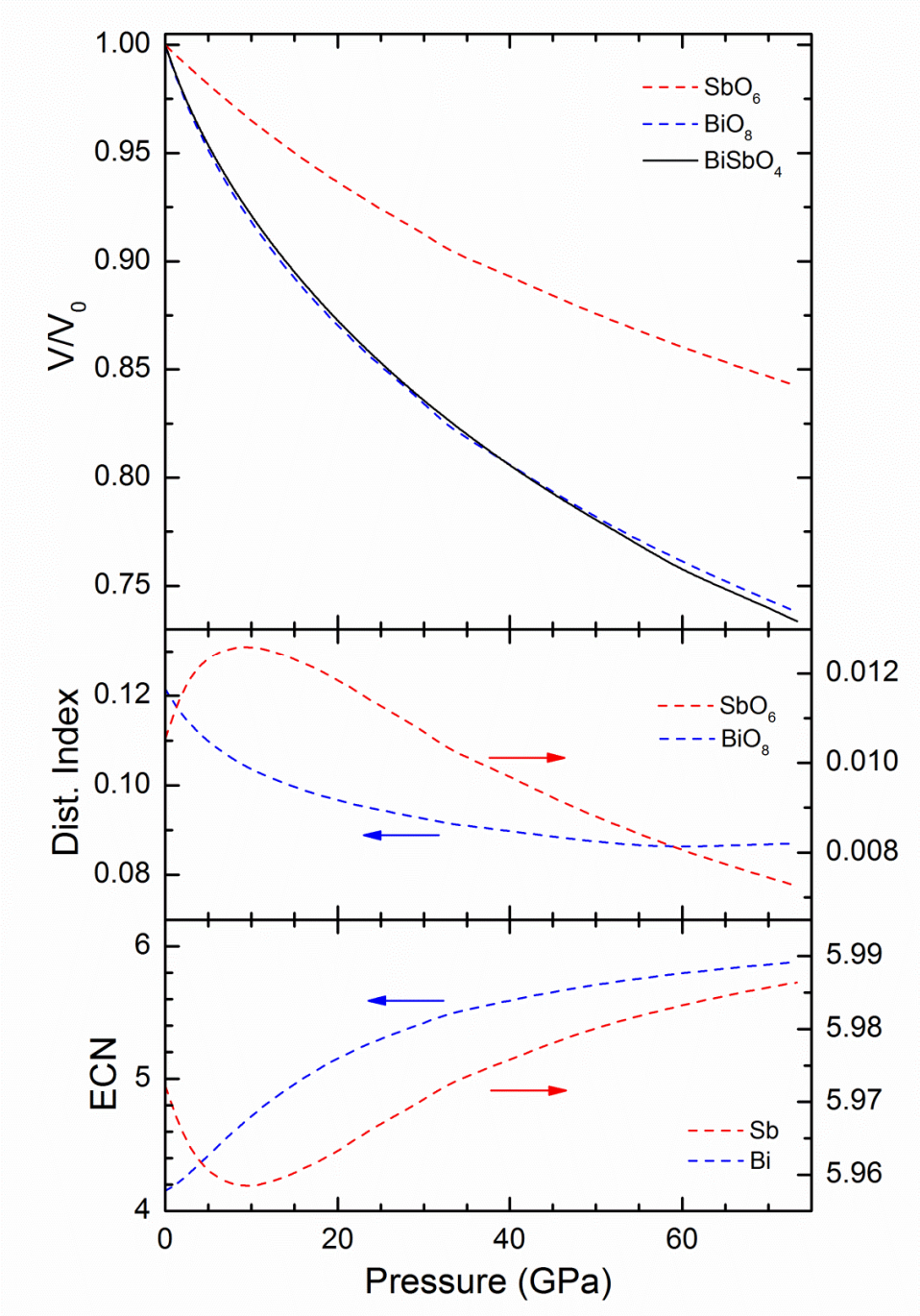
1.00
0.95
0.90
0.85
0.80
0.75
V/V0
SbO6
BiO8
BiSbO4
0.12
0.10
0.08
Dist. Index
SbO6
BiO8
0.012
0.010
0.008
6
5
4
ECN
Sb
Bi
5.99
5.98
5.97
5.96
0
20
40
60
Pressure (GPa)

Figure 11

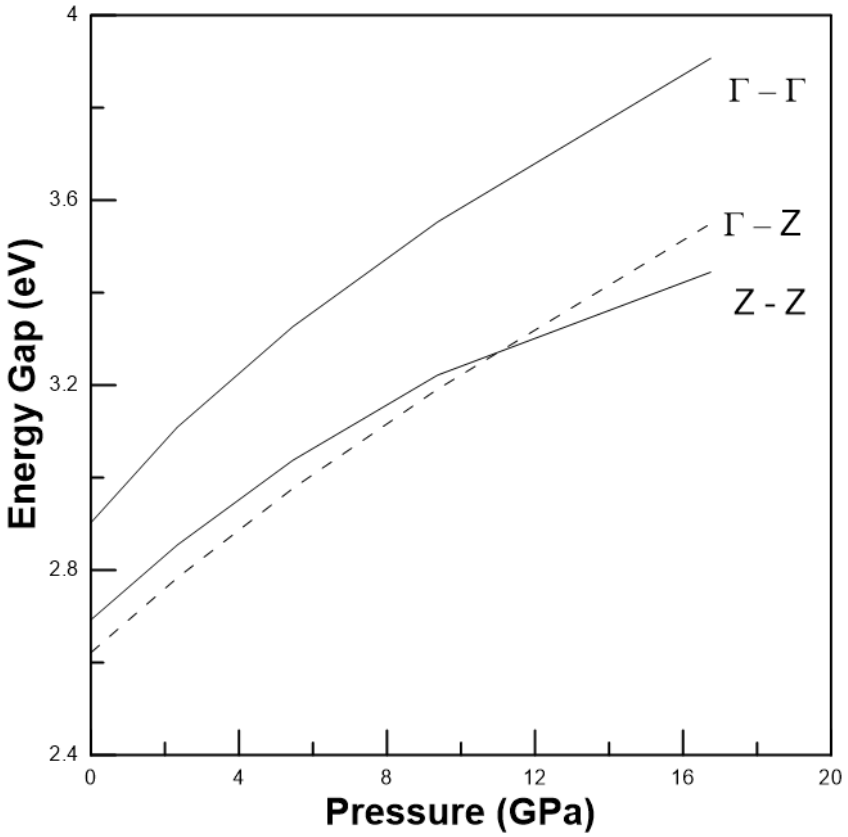

Figure 12

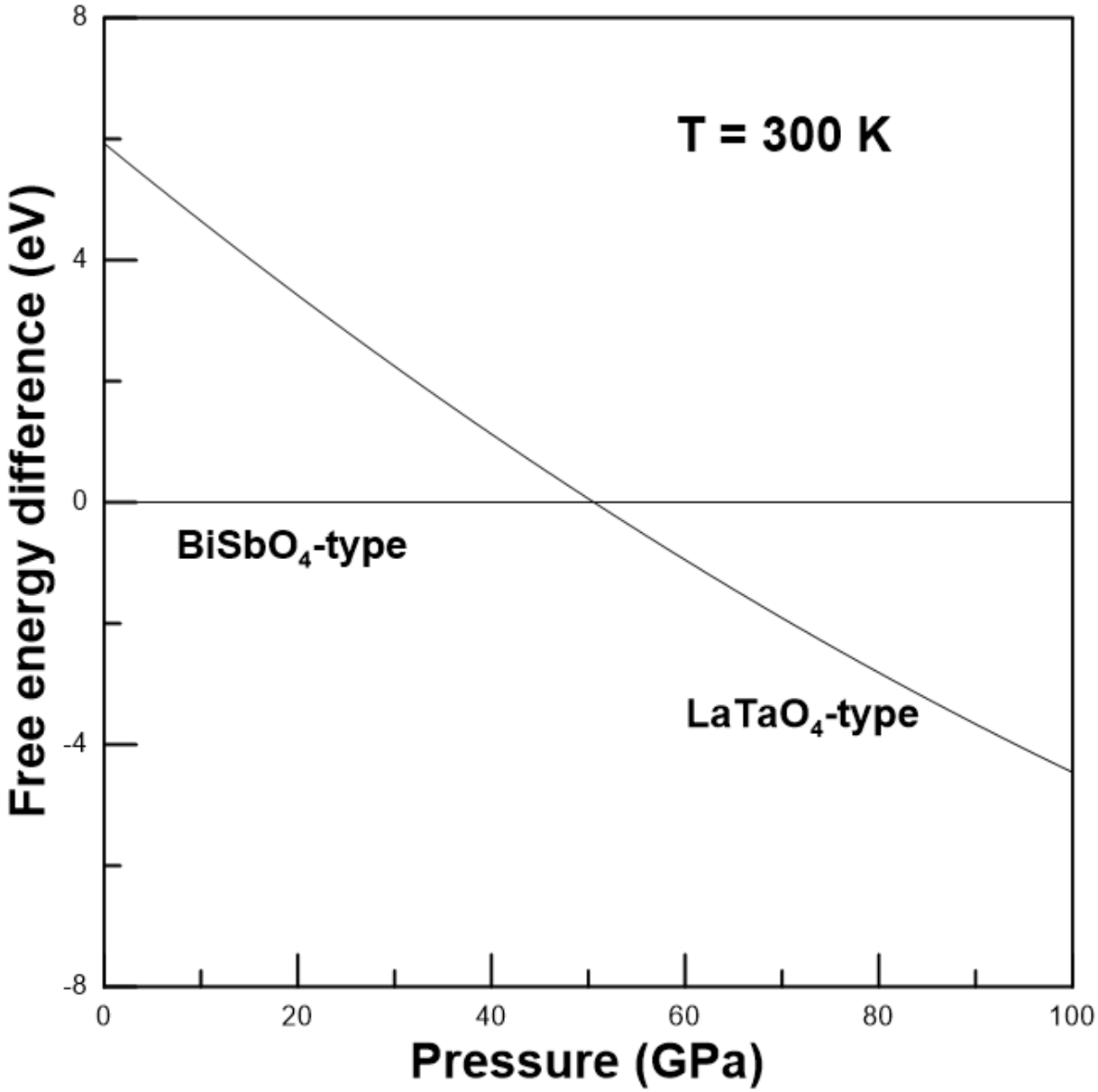
T = 300 K
Free energy difference (eV)
8
4
0
-4
-8
BiSbO4-type
LaTaO4-type
0
20
40
60
80
100
Pressure (GPa)

Table of Contents

The high-pressure structural, electronic, and vibrational properties of $BiSbO_4$ were studied experimentally and theoretically for the first time up to 70 GPa. The crystal structure, Raman and IR modes, as well as the band structure of $BiSbO_4$ are accurately described as well as the influence of pressure in them. The room-temperature equation of state and the isothermal compressibility tensor are reported. A possible high-pressure phase is proposed based upon numerical simulations. The reliability of the results is supported by the consistency between theory and experiments.